Biosensors and Bioelectronics 126 (2019) 136–142

Contents lists available at ScienceDirect

Biosensors and Bioelectronics

journal homepage: www.elsevier.com/locate/bios

Reduced graphene oxide biosensor platform for the detection of NT-proBNP biomarker in its clinical range

Walid-Madhat Munief[a,b,c,*,1], Xiaoling Lu[a,f,1], Tobias Teucke[a], Jannick Wilhelm[c], Anette Britz[a], Felix Hempel[c], Ruben Lanche[c], Miriam Schwartz[c], Jessica Ka Yan Law[c], Samuel Grandthyll[g], Frank Müller[g], Jens-Uwe Neurohr[g], Karin Jacobs[g], Michael Schmitt[e], Vivek Pachauri[a,f], Rolf Hempelmann[b,d], Sven Ingebrandt[a,f]

[a] Department of Informatics and Microsystem Technology, University of Applied Sciences, Kaiserslautern, 66482 Zweibruecken, Germany
[b] Department of Physical Chemistry, Saarland University, 66123 Saarbruecken, Germany
[c] RAM Group DE GmbH, Research and Development Center, 66482 Zweibruecken, Germany
[d] Korean Institute of Science and Technology, 66123 Saarbruecken, Germany
[e] Institute for Coatings and Surface Technology, University of Applied Sciences Niederrhein, 47805 Krefeld, Germany
[f] Department of Electrical Engineering and Information Technology, IWE 1, RWTH Aachen University, 52074 Aachen, Germany
[g] Department of Experimental Physics, Saarland University, Campus E2.9, 66123 Saarbruecken, Germany

ARTICLE INFO

Keywords:
Reduced graphene oxide (rGO) thin-films
New reduction concept
rGO ion sensitive field-effect transistor (ISFET) biosensor
Detection of NT-proBNP in the clinical range

ABSTRACT

Reduced graphene oxide (rGO) thin films can be exploited as highly sensitive transducer layers and integrated in interdigital micro-electrode systems for biosensing processes. The distinctive bipolar characterisitics of rGO thin films can be modulated by a very low external electric field due to the electrostatic charges of biomolecules. These charges lead to a fast response in the readout signals of rGO based ion sensitive field-effect transistors (ISFETs). The characterisitc changes of rGO ISFETs enable a fast, accurate and reproducible detection of biomolecules. The biosensing mechanism offers a fast and label-free approach for analyte detection in contrast to the classical ELISA method.

In this contribution, we introduce a reproducible fabrication process of rGO based field-effect transistors on wafer level. The sensors are functionalized as biosensors to measure N-terminal pro-brain natriuretic peptide (NT-proBNP) in human serum within its clinical range. Our optimized rGO sensor shows very promising electrical properties and can be considered as a proof of concept study for the detection of various analytes. The easy and cost-effective fabrication as well as the versatile usability make this new technological platform an auspicious tool for different sensing applications in future.

1. Introduction

The development of sensor systems with the ability to detect antigens in low concentration ranges has been an uninterrupted interest for clinical studies as well as scientists in the field of biosensors (Li et al., 2013; Song et al., 2017). Since the 1960s, versatile methods have been established and consequently improved to detect specific antigens for biosensing research. One of the most reliable techniques today is the Enzyme-linked Immunosorbent Assay (ELISA) (Garcia et al., 1998; Hnasko et al., 2011). ELISA serves as a well-established and well-understood method, which is already used in hospitals and analytical labs for the detection of proteins, viruses, hormones and toxins (Sabzwari and Slade, 2017;Song et al., 2017; Zhuo et al., 2011). ELISA is a fluorescence based optical method, which requires elaborated mechanisms in order to identify the analyte in solution (Li et al., 2016). This optical method exhibits a major disadvantage while analyzing low concentrations of antigen biomarkers, due to the fact that the optical resolution is obstructed by physical laws. In addition, a high analyte volume is needed, fluorescence labels are required, and the measurement time is long (Garcia et al., 1998; Pan et al., 2017). These limitations do not allow for fast medical and early-stage diagnostics. Due to these facts, technological alternatives for fast, reliable, cost-effective and label-free sensors are currently in high demand. In the field of electrical sensing, there is an increased desire to develop efficient

* Corresponding author at: Department of Informatics and Microsystem Technology, University of Applied Sciences, Kaiserslautern, 66482 Zweibruecken, Germany.
[1] Contributed equally as the first author to this work.

https://doi.org/10.1016/j.bios.2018.09.102
Received 12 July 2018; Received in revised form 22 September 2018; Accepted 29 September 2018
Available online 17 October 2018
0956-5663/

biosensors with superior capabilities for early state diagnostics, which are not attainable through optical assays (C.H. et al., 2017; Hancock and Tsang, 1986; Zhuo et al., 2011; Zhang and Shu, 2017; Wang et al., 2011).

Graphene oxide (GO) is a carbon-based material that has gained plenty of attention in the last decade (Novoselov et al., 2012; Eigler, 2016; Nair et al., 2008; Feng et al., 2018). It is biocompatible and can be used as a highly sensitive transducer layer integrated in an ISFET configuration. rGO thin films, in particular, possess bipolar behavior and offer high biocompatibility (Boscher et al., 2010; Cai et al., 2014; Stebunov et al., 2015). In terms of electrical properties, rGO exceeds the properties of silicon devices (Rani et al., 2016). Furthermore, the fabrication of rGO devices is easy and cost-effective (Hess, 2013; Wang et al., 2011).

In this contribution, the electrical detection of the biomarker NT-proBNP in human blood serum within its clinical range is shown as a proof of concept (Lu et al., 2018a, 2018b; Mao et al., 2011; Zhuo et al., 2011), (Seshadri et al., 2018). This biomarker, a peptide secreted by the heart muscle cells in case of excessive strain can be used to identify a heart failure (Gustafsson et al., 2005). A fast detection of NT-proBNP is not possible based on existing methods (Stebunov et al., 2015). A label-free and fast detection of NT-proBNP would be valuable for patients around the world (Saenger et al., 2017). The proposed platform offers a fast and reliable analysis and could be empolyed as an early stage diagnostic setup for addressing the biomarkers of heart diseases in the clinical range. Combined with a low-cost fabrication process, the established platform is potentially valuable for medical science as well as for biosensing applications.

2. Materials and methods

2.1. Fabrication of rGO-ISFET sensor

The syntheses of GO flakes is based on an already established low-temperature exfoliation and desalination (LTED) protocol (Lu et al., 2018a, 2018b; Eigler and Hirsch, 2014). The lithography processes were performed as explained in previous publications (Lu et al., 2018a, 2018b). The wafer surface was modified by gas phase silanization evaporation with (3-aminopropyl) triethoxysilane (APTES, Sigma Aldrich, Germany), (Munief et al., 2018; Schmitt and Heib, 2013; Schmitt, 2014). On this condensate layer of aminopropylsiloxane (APS), the GO aqueous solution was spin coated 3 times and the formed GO thin films were micro-structured via photolithography and dry etching with O_2-plasma (100 W, 13 Pa, 20 s, SI 591 M, Sentech GmbH, Germany). Except the area of GO patterns and contact pads, all the conductive lines were passivated with a new borosilicate glass procedure. With a rapid thermal processing (RTP-CVD reactor, ASOne150, ANNEALSYS, France), the GO was reduced to rGO in 1 s at 450 °C (Phan and Chung, 2015). Each wafer contained in total 100 rGO-IDEs devices.

The rGO pattern under the IDEs serves as gate area, which is of a size 200 μm × 200 μm. Each rGO-IDEs chip consisted of a 4 × 4 pattern of gates with 8 gold electrodes as the source contacts and another 8 gold electrodes as the drain contacts (L = 3200 μm) (Fig. 1a). The rGO-ISFETs have an effective gate width of W = 200 μm and an effective gate length of L = 5 μm. The separated chips were wire bonded to chip carriers (LeitOn GmbH, Germany) and encapsulated with glass rings using silicone adhesive (Dow Corning, 96-083) in order to generate a reservoir and enable measurements in liquid. The wire bonds were covered by a layer of the silicone adhesive to avoid electrical short circuits.

2.2. Material characterization of GO/rGO

The X-ray photoelectron spectroscopy (XPS) experiments were performed with an ESCA Lab MK II by Vacuum Generator using a non-monochromatised X-ray source (Al-Kα, ħω = 1486.6 eV). The C-1s spectra were recorded in normal emission at a pass-energy of 10 eV.

Raman spectra were recorded using a Raman Microscope (LabRAM HR Evo-Nano, HORIBA Jobin Yvon GmbH) with an excitation wavelength of 630 nm. A grating with 2400 lines/mm, and a 100× objective (numeric aperture: 0.9) were used. The spectral resolution was ~ 1.2 cm^{-1}, and the spot size on the sample mounted in the focal plane ~ 2 μm using an output power of 0.3 mW. The acquisition time was 30 s to eliminate cosmic rays and to improve the signal-to-noise ratio. We used the Gaussian-Lorentzian algorithm to deconvolute the peak position which is essential to track the change in the layer properties after the thermal treatments. Hence, we iterated the four important Raman GO/rGO signatures: the D band assigned as the A_{1g}-mode of the displacement, the G bands as the Raman active E_{2g} mode, the D" provides the assumption about the content of oxygen atoms and the second order 2D bands describe the symmetry or non-symmetry of the crystal lattice (Cançado et al., 2011; Ferrari and Basko, 2013).

The scanning electron microscope (SEM) imaging of the samples was carried out on a Supra40 microscope (ZEISS AG, Germany), in low voltage mode at 5 kV and 10 mm working distance using a 20 mm size aperture. High magnification images were taken at 4.45 kV (magnification in reference to device output 2700 screen). The pixel resolution was 66.2 nm. All pictures were taken using an Everhard Thornley type SE-detector (detection for secondary electrons), to reveal the topographic features on the sample surfaces by edge effect and shadow formation.

2.3. Characterization setup for the field-effect measurements

The field-effect measurements were done with a semiconductor parameter analyzer (Keithley 4200-SCS, Tektronix GmbH, Germany). Drain-source voltages (V_{DS}) were swept from −0.6 V to + 0.3 V. A gate-source voltage (V_{GS}) of 0.1 V was applied between the gate and source electrodes with a step size of 0.1 V. To investigate the influence the change of the V_{GS} on the I_{DS}, different V_{GS} voltages (- 0.3 V, - 0.2 V, - 0.1 V, - 0.05 V, - 0.01 V to + 0.01 V, + 0.05 V, + 0.1 V, + 0.2 V, + 0.3 V) were applied.

2.4. Assay preparation for the NT-proBNP detection

The rGO surface was treated with a mixture of 80 mM (1-ethyl-3-(3-dimethylaminoprpyl) carbodiimide (EDC), (E1769, Sigma-Aldrich, Germany) and 20 mM N-hdydroxysuccinimide (NHS), (130672-5G, Sigma-Aldrich, Germany) with a volume ratio of 1:1. The rGO-ISFET chips were incubated with the EDC/NHS solution for 30 min at room temperature. Afterwards, the EDC/NHS solution was removed and the rGO chips were cleaned with 1 ml DI water and 1 ml phosphate buffered saline (PBS, P4417-50TAB, Sigma-Aldrich, Germany) three times. The antibodies (10 μg/ml, monoclonal antibody 4NT1–11D1, human antibody Mab:11D1, HyTest Ltd., Finnland) were incubated over night at 4 °C. In the next step, the antibody solution was removed and the chips were cleaned three times with 1 ml DI water and three times with 1 ml PBS. After this, the free activated surface groups were blocked with ethanolamine (ETA), E9508 Sigma-Aldrich, Germany). The incubation was performed in 10 mM ETA for 30 min at pH ~ 7.4. Then, the chips were cleaned with 1 ml DI water and finally 1 ml PBS. The antigen was mixed into a human serum sample solution (Cat.# 8NT2 BNP and proBNB recombinant human plasma, HyTest Ltd., Finnland) and was added to the devices in different concentrations (0,1 pg/ml, 1 pg/ml, 10 pg/ml, 100 pg/ml, 1000 pg/ml, 5000 pg/ml and 10000 pg/ml). All measurements of NT-proBNP were performed with an Ag/AgCl reference electrode (DRIREF-2SH, World Precision Instruments, Germany) in solution.

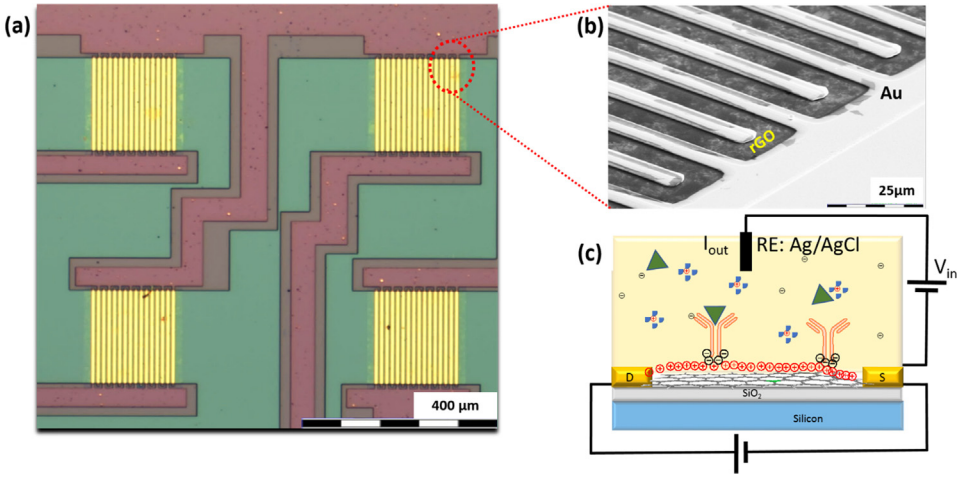

Fig. 1. (a) Optical differential interference contrast image of four interdigitated electrode (IDE) sensor spots out of a 4 × 4 channel chip array. The conductive lines are passivated with a new established borosilicate passivation. (b) The graphene oxide layer was patterned and afterwards contacted by gold electrodes in an IDE configuration. GO was reduced to rGO to enable an electronic carrier transport through the material. (c) Schematics of the biosensor interface architecture. Reduced graphene oxide is modified with antibodies against NT-proBNP. The ionic composition of the test solution and the interface architecture of the biomolecules attached to the sensor surfaces leads to a specific ionic composition at the rGO-liquid interface. The EDL acts as the 'gate dielectric' material for the rGO field-effect transistor characteristics.

3. Results

3.1. Material characterization of GO and rGO

The central aspect for the later electrical performance of these specific sensors is the high precision spin coating of the GO to create ultra-thin films with an average thickness of 1.5–2.5 nm over a four-inch wafer. This thickness is the key parameter to produce such high sensitive transducer layers with a very low limit of detection. The SEM micrograph (Fig. 1(b)) illustrates the highly precise and homogenous integration of the IDEs and the GO layers. The layers are agglomerated without grain boundaries to an average thickness of 2 nm. The influence of the thermal treatments on the GO/rGO layers was characterized by Raman spectroscopy and XPS (Fig. 2(a) - (d)). According to fundamental results of previous basic studies, we are able to differentiate the structure evolution of the thin-film layer after thermal reduction with the Raman microanalysis (Fig. 2(b), (d)) by the shift of the peak position, the full width at half maximun (FWHM) as well as the intensity (Cançado et al., 2011; Ferrari and Basko, 2013; Dresselhaus et al., 2010; Jorio et al., 2011). Additionally, the XPS data provides information on the overall amount of carbon in the thin-film, the formation of oxygen, as well as the amount of oxygen bonded carbon. The sheet homogeneity of the IDE channel after the spectroscopy analysis was electrically confirmed with a I-V dual-sweep.

Fig. 2(b) and (d) show the D peak position for GO allocated at 1325 cm^{-1} and for rGO at 1330 cm^{-1}. The corresponding FWHM value decreased after reduction from 110 to 90 and the intensity decreased from 95.7% to 90.1%. A comparable tendency is set by the first order G-peak which is assigned for GO at 1601 cm^{-1} and for rGO at 1608 cm^{-1}, where the appearing normalized intensity increased from 81% to 92% whereas the FWHM decreased from 54 to 48. A closer consideration of the D" band shows that the GO fit is allocated at 1527 cm^{-1} and for rGO at 1581 cm^{-1} with the corresponding decrease in FWHM (Socrates, 2004) from 207 to 76 and the intensity increase from 18.1 to 28.4. Furthermore, a similar situation can be observed regarding the second order 2D band which appears for GO at 2638 cm^{-1} and for rGO at 2622 cm^{-1} and the FWHM decreased from 136 to 133 and the normalized intensity increased from 2.4% to 2.6% (Socrates, 2004).

The reduction concept is based on the amount of the different carbon species on the atomic level (e.g. C-C, C-O and C=O) before and after the thermal treatment (Fig. 2(a) and (c)). These experiments were performed on non-reduced GO samples as well as on rGO samples where the substrate was annealed at 450 °C. For the non-reduced GO sample, the XPS data shows mainly signals from C, O and the Si substrate with C: O: Si = 21.0 at%: 50.8 at%: 28.2 at%. In comparison, the elemental composition for rGO changes to C: O: Si = 17.0 at%: 52.9 at %: 30.1 at% with the relative decrease of C resulting from the elimination of additional C related adsorbates. The comparison between the GO and rGO indicates the transformation of the material properties on the crystal plane lattice (Beamson and Briggs, 1993; Delle et al., 2015).

To confirm the uniformity of the rGO sheet, the I-V dual-sweep configuration (Fig. 2(e)) was used to analyze the channel function and the electrical variation of the channels. After the reduction, the ohmic contact between the rGO thin-film and the IDT is confirmed for all 16 channels by a linear current-voltage characteristic curve. The rGO-ISFET chips show a typical resistance behavior for amorphous rGO with values of around 40 kOhms ± 9% with an applied bias voltage of 100 mV.

The investigation of rGO shows the transformation of the material properties on the crystal plane lattice (Beamson and Briggs, 1993; Delle et al., 2015). A significant number of functional groups which serve as potential binding sites as well as the chemical and electrical homogeneity are essential for the detection of different NT-proBNP concentrations.

3.2. Electrical characterization of the rGO-ISFET

To apply the rGO thin films as transducer layers in ISFET devices for biosensor applications, the electronic performance and the thin-film homogeneity were evaluated in detail. The bipolar behavior of the devices was investigated experimentally (Fig. 3). The Dirac point was tuned with different gate voltages. Also, the shift of the Dirac point was observed to be influenced by varying pH values and ionic strengths in PBS solutions. The performed measurements are necessary to comprehend the biosensing mechanism of rGO based ISFET devices.

An exemplary characteristic curve of the rGO based ISFET devices is shown in Fig. 3(a). The left arm of the bipolar curve shows the region of the hole mobility while the right arm shows the region of the electron mobility. According to the curve, the carrier concentration of holes is higher, which may lead to a steeper curve at the left arm of the bipolar function.

Fig. 3(b) shows the influence of different V_{GS} on the Dirac point and I_{DS}. Different V_{GS} were applied from −0.6 to + 0.4 V in steps of 0.1 V. The V_{GS} variation changes the I_{DS} which can be considered as a fine-tuning of the Fermi level in the rGO layer. The Fermi level can be allocated at the Dirac cones in which the I_{DS} achieves the minimum current flow close to zero. That phenomenon is mainly caused by the valence and conductance band taking over the shape of the upper and the lower half conical band structures so that they meet at this position, (Partoens and Peeters, 2006; Hess et al., 2013). However, the Dirac cones describe the behavior of the charge carrier mobility through the rGO thin-film and show the change of the Fermi level by tuning the V_{GS} (Morozov et al., 2005). In the rGO thin-film, the carrier transport is

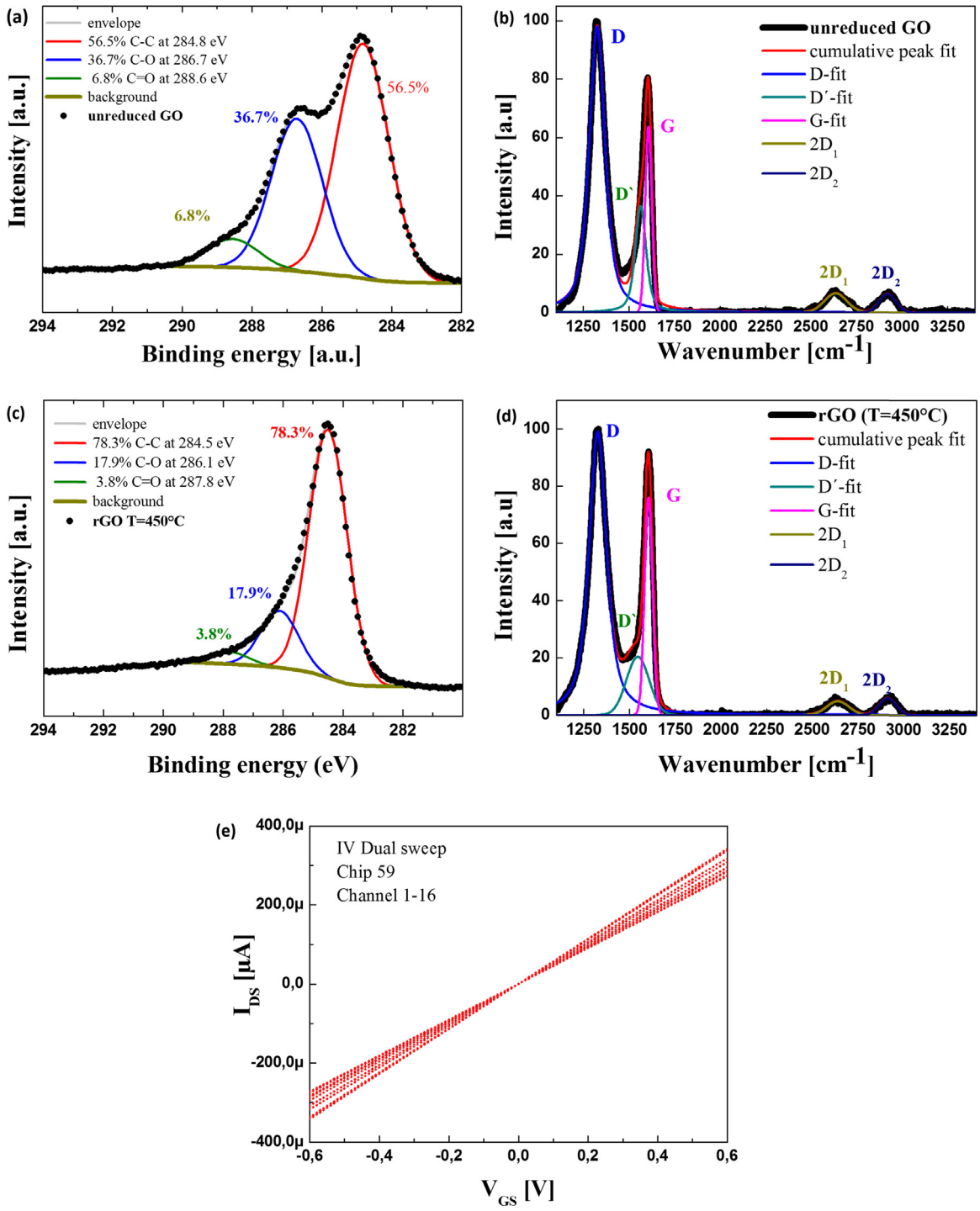

Fig. 2. XPS after the Shirley background correction of the photoemission to compare (a) the GO before and (c) after the thermal treatment. Raman spectroscopy shows the molecular vibration mode of the (b) unreduced GO thin-film and (d) after the rapid thermal processing reduction. (e) The I-V dual-sweep confirms the linear characteristic trend of 16 channels after the reduction. This demonstrates that the ohmic contact is formed between rGO and the IDEs and that the transducer layer is homogenous.

based on the hopping from the source electrode through the transducer layer towards the drain electrode. The Dirac point is located at negative V_{GS} close to $V_{GS} = 0$ V where I_{DS} has its lowest value. The location of the Dirac point in negative V_{GS} demonstrates the p-type behavior of the rGO thin film. The variation of the V_{GS} from negative to positive bias voltage shows a symmetric shifting of the Dirac point (Fig. 3(b)) and confirms the p-type behavior of the rGO thin-film.

The sensor response for different pH solutions is shown in (Fig. 3(c)) at $V_{GS} = +0.1$ V. The Dirac point drastically shifted by the change of the electrostatic double layer capacitance during the variation of the pH solutions from pH 6–6.5, 7, 7.5 and 8. For the acidic pH values, the Dirac point shifts to lower V_{GS} when compared to pH 7. The alkaline pH solutions show a shift in the opposite direction. A change of 40 mV/pH can be seen. In order to test the long-term stability of the rGO sensors, the devices were tested in 150 mM PBS solution.

As illustrated in Fig. 3(d), the influence of different ionic strengths from 10 mM, 25 mM, 50 mM, 75 mM, 100 mM, 125 mM and 150 mM PBS on the rGO devices was determined. The different applied ionic

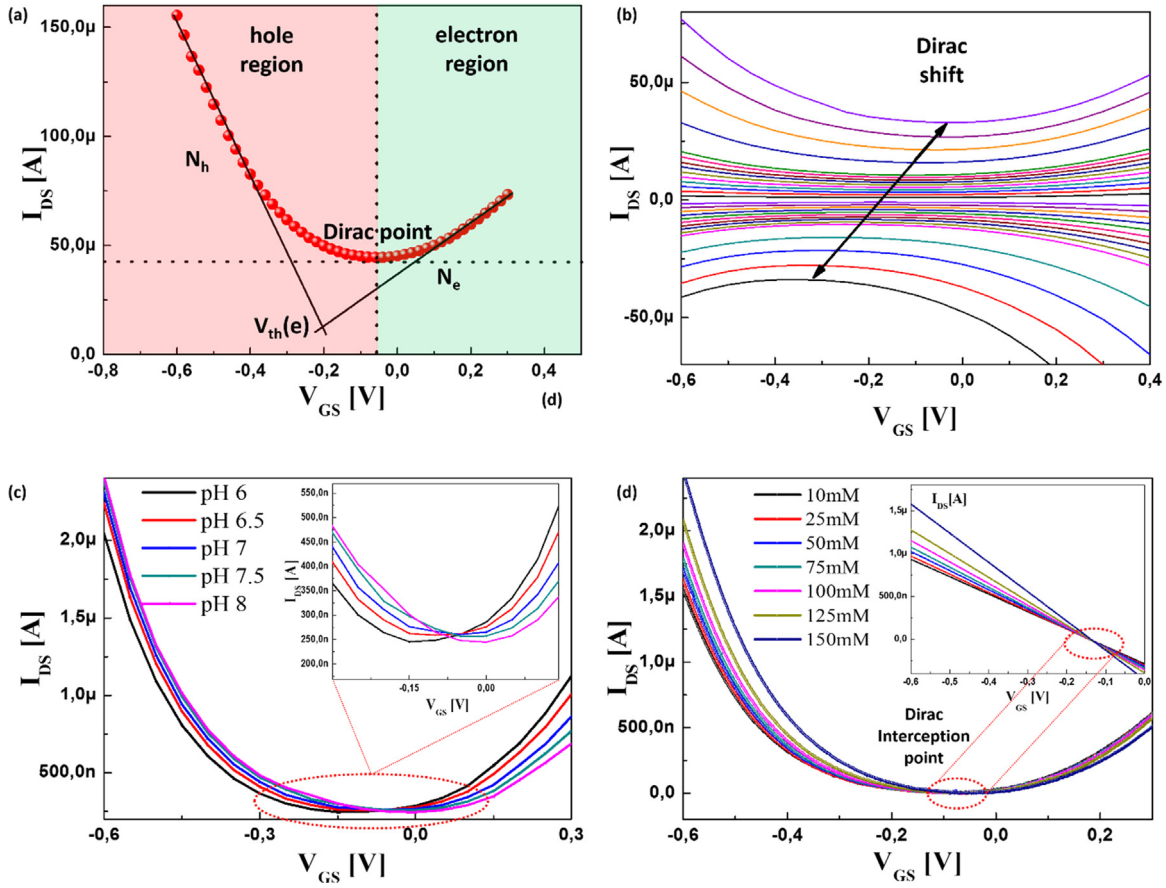

Fig. 3. (a) Bipolar transport property of the rGO-ISFET device. The left arm shows the hole carrier region and the right arm the electron region. An extrapolation of both linear regions in this plot reveals the respective threshold voltages V_{th} (h) and V_{th} (e). (b) The tuning of different V_{GS} shows a symmetric shift of the Dirac point in the bipolar characteristic curve of the rGO-ISFETs. (c) Localization of the Dirac point by different pH solutions. (d) The intersection of the Dirac points is constant after adding the solutions with different ionic strengths, while I_{DS} still changes.

concentrations are modulating the surface potential of the electrostatic double layer (EDL) capacitance on the transducer layer. The change of higher or lower ionic concentrations creates the potential difference between the interface of the bulk solution and the solid carbon layer. The charges at the phase boundary are compensated by a number of charge carriers in the aqueous phase which is modulating the carrier density in the rGO thin films at the hole transport region.

The changes of the bipolar curves after the baseline correction are caused by the potential difference of different buffer concentrations. The shift of the Dirac point is infinitesimal. The gradient of all bipolar functions is shown in Fig. 3(d). The calculated intersection of the Dirac points after adding the different concentrations is in the range from - 0.09 V to - 0.06 V. This is neglectable in comparison to the response behavior of the p-type region. This characteristic result is similar to the studies based on graphene devices (Kim et al., 2013). The ionic charges of the bulk solutions do not influence the Dirac point, but the shift of the bipolar curve function is still possible. The p-type function confirms the conductivity of the rGO and must be considered as the response region for the sensing procedure under assay conditions. Based on this response effect of the rGO devices, a selective sensing performance in physiological buffer was achieved, which is essential for the assay analysis.

3.3. Biosensing of NT-proBNP biomarker

Different concentrations of NT-proBNP were tested with the rGO-ISFET. Fig. 4 illustrates the field-effect measurements of different channels after the raw data was baseline corrected over the local minimum of the Dirac point (Fig. 4(a)). The I_{DS} change in the bipolar curve of the rGO devices is the sensor response. The Dirac point can be considered as constant and does not influence the sensor detection. The applied concentrations of NT-proBNP were in the clinical relevant range for the early stage detection of the peptide. Table 1 gives an overview about the performance of the existing scientific platforms as well as commercial available ELISA kits for NT-proBNP detection.

The starting values of the field-effect measurements are calculated for the clinical relevant range for early stage diagnosis. To determine the I_{DS} changes dependent on the biomarker concentration, the gradient of the bipolar function was calculated (Fig. 4(b)). Additionally, the intersection of the Dirac points after adding the different concentrations of the NT-proBNP biomarkers confirm that the shifting only occurs in the small range from -0.095 V to -0.087 V. The comparison of the response behavior illustrates that the I_{DS} conductance decreases at the p-type curve function within the range from 1.16 µS to 700 nS at V_{GS} = 0.6 V. The Dirac shift has no noteworthy influence on the measurement. The complex formation between the antibodies and the antigens is accompanied by the decrease of the current I_{DS} at the hole region side on top of the rGO layer. The sheet resistance of the rGO-ISFET transducer layer increases during the binding reaction of the different biomarker concentrations and leads to the lower of the bipolar function.

Furthermore, the obtained changes of the field-effect measurements of five different channels with NT-proBNP are evaluated in a concentration-response graph (Fig. 4(c)). The results indicate that the lowest concentration of antigens that can be detected is in the range of 1–10 pg/ml. Above 1000 pg/ml peptide, the saturation point was observed (Zhang and Shu, 2017; Garcia et al., 1998). The used Michaelis-

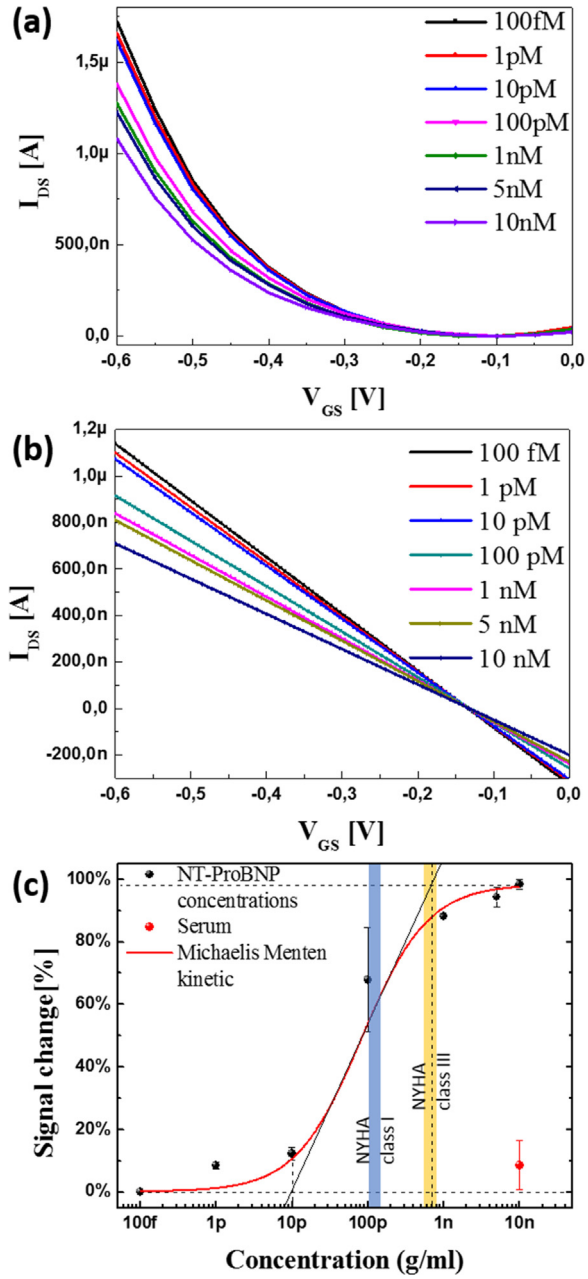

Fig. 4. (a) Baseline corrected p-type curve function with different NT-proBNP concentrations. The specific binding of the biomarker to the antibody increases the sheet resistance while the Dirac point is constant. (b) The gradient corresponds to the instantaneous change of the bipolar waveform by the addition of different antigen concentrations. (c) Plot of the binding isotherm with different antibody concentrations in 150 mM serum buffer. The sensor is reacting in the clinically-relevant range at 100 pg/ml (blue frame) and is within the class I region according to the NYHA definition. The yellow bar illustrates class III according to the NYHA.

Menden function can be considered as an approximation to calculate the limit of detection (LoD) value with 10 pg/ml of NT proBNP. The calculated LoD is 30 pg/ml (calculation based on DIN 32645). This value is below the threshold value of the New York Heart Association (HYHA) at stage 1 (100 pg/ml for men and 125 pg/ml for women) and allows an assertion about the health condition of the patient (Maisel, 2001). The upper LoD is 713 pg/ml, which is slightly above the NYHA stadium III and can therefore be considered as the value of acute and severe heart failure (Raphael et al., 2007).

The measurements show a clear change in I_{DS} due to the binding of NT-proBNP to its specific antibody. In comparison to the experimental bipolar function, it is obvious that the decrease of the I_{DS} is caused by the specific binding between the antibody and the antigen. At the measured protein concentration of 100 pg/ml, the senor response corresponds the clinical range of NT-proBNP.

Table 1
Comparision of the limit of detection and the detection range of scientific developments and commercialised systems for NT-proBNP detection.

Sensing mechanism for NT-proBNP detection	*Limit of detection (pg ml^{-1})*	*Detection range (pg ml^{-1})*	*Reference*
Electrochemical	*6*	*20–100000*	(Zhuo et al., 2011)
Chromathography	*47*	*200–26000*	(Li et al., 2016)
Luminiscence	*17*	*–*	(Zhang and Shu, 2017)
Fluorobead label	*3.7*	*7–600*	(Song et al., 2017)
Commercial ELISA	*30.9*	*30–2500*	ABIN4947956
Commercial ELISA	*46.88*	*3000*	ABIN5706197
Commercial ELISA	*50*	*50–1000*	ABIN511239
Commercial ELISA	*140*	*140–100000*	ABIN1979532

4. Conclusion

With this proof of concept study we introduced an innovative rGO sensor platform, in which NT-proBNP could be measured with a very low limit of detection. The dose response measurements showed that the clinical range for the NT-proBNP was covered in the linear range based on the definition of the New York Heart Assiocitation for heart failure. Only the preparation of rGO ultra thin-films enables this platform such a high performance for biosensing applications. We showed a cost-effective, reliable, sensitive, selective and reproducible way to detect antigens within the physiological buffer serum. When compared to the traditional methods such as the ELISA kits, the label-free detection as well as the fast response time of less than 15 min with small sample volumes of 50 µl show some impressive advantages. However, to realize clinical applications with the proposed devices, additional improvements are required. Until now it is not possible to reutilize such a sensor after the measurement under human serum condition. Furthermore, the rapid detection of NT-proBNP for early-stage diagnosis requires an optimized assay to reduce errors. Nevertheless, a strong performance of the devices was shown as well as a potential platform for other biosensor applications, since the measurement principle can be easily transferred to other fields, such as DNA or gas sensing, etc. In future work for industrial applications the rGO transducer performance can be further improved if the large area thin-film consists exclusively of GO monolayers. Such enhancement of the rGO ISFET transducer layer could provide an alternative platform to compete with already established and commercially available ELISA kits.

Acknowledgements

Xiaoling Lu was funded by the European Commission Program through the Marie Curie Initial Training Network PROSENSE EU FP7 ITN (grant no. 317420, 2012–2016, www.prosense-itn.eu). W.M.M acknowledge the support from Euroimmun Medizinische Labordiagnositika AG, Lübeck, Germany. The authors thank Detlev Cassel and Rainer Lilischkis (both University of Applied Sciences Kaiserslautern, Germany).

References

Beamson, G., Briggs, D., 1993. High resolution XPS of organic polymers: the scienta ESCA300 database. J. Chem. Educ. 70, A25. https://doi.org/10.1016/0368-2048(93)85006-7.

Boscher, N.D., Choquet, P., Duday, D., Verdier, S., 2010. Chemical compositions of organosilicon thin films deposited on aluminium foil by atmospheric pressure dielectric barrier discharge and their electrochemical behaviour. Surf. Coat. Technol. 205,

2438–2448. https://doi.org/10.1016/j.surfcoat.2010.09.037.
C.H, H., D., Y, M.A., K., W.P, W., 2017. Nanoswitch-linked immunosorbent assay (NLISA) for fast, sensitive, and specific protein detection. Proc. Natl. Acad. Sci. USA 114, 10367–10372. https://doi.org/10.1073/pnas.1708148114.
Cai, B., Wang, S., Huang, L., Ning, Y., Zhang, Z., Zhang, G.J., 2014. Ultrasensitive label-free detection of PNA-DNA hybridization by reduced graphene oxide field-effect transistor biosensor. ACS Nano 8, 2632–2638. https://doi.org/10.1021/nn4063424.
Cançado, L.G., Jorio, A., Ferreira, E.H.M., Stavale, F., Achete, C.A., Capaz, R.B., Moutinho, M.V.O., Lombardo, A., Kulmala, T.S., Ferrari, A.C., 2011. Quantifying defects in graphene via Raman spectroscopy at different excitation energies. Nano Lett. 11, 3190–3196. https://doi.org/10.1021/nl201432g.
Delle, L.E., Huck, C., Bäcker, M., Müller, F., Grandthyll, S., Jacobs, K., Lilischkis, R., Vu, X.T., Schöning, M.J., Wagner, P., Thoelen, R., Weil, M., Ingebrandt, S., 2015. Impedimetric immunosensor for the detection of histamine based on reduced graphene oxide. Phys. Status Solidi Appl. Mater. Sci. https://doi.org/10.1002/pssa.201431863.
Dresselhaus, M.S., Jorio, A., Saito, R., 2010. Characterizing graphene, graphite, and carbon nanotubes by Raman spectroscopy. Annu. Rev. Condens. Matter Phys. 1, 89–108. https://doi.org/10.1146/annurev-conmatphys-070909-103919.
Eigler, S., 2016. Graphene synthesis. In: Graphene Technology: From Laboratory to Fabrication, pp. 19–61. ⟨https://doi.org/10.1002/9783527687541.ch2⟩.
Eigler, S., Hirsch, A., 2014. Chemie an Graphen und Graphenoxid – eine Herausforderung für Synthesechemiker. Angew. Chem. 126, 7852–7872. https://doi.org/10.1002/ange.201402780.
Feng, Q., Zhao, X., Guo, Y., Liu, M., Wang, P., 2018. Stochastic DNA walker for electrochemical biosensing sensitized with gold nanocages@graphene nanoribbons. Biosens. Bioelectron. 108, 97–102. https://doi.org/10.1016/j.bios.2018.02.050.
Ferrari, A.C., Basko, D.M., 2013. Raman spectroscopy as a versatile tool for studying the properties of graphene. Nat. Nanotechnol. 8, 235–246. https://doi.org/10.1038/nnano.2013.46.
Garcia, H.H., Harrison, L.J.S., Parkhouse, R.M.E., Montenegro, T., Martinez, S.M., Tsang, V.C.W., Gilman, R.H., Tovar, M., Rodriguez, S., Alvarado, M., Nunez, J., Portilla, L., Valencia, A., Torres, L., Verastegui, M., Herrera, G., Gonzalez, A.E., Gavidia, C., Falcon, N., Bernal, T., Evans, C.A.W., 1998. A specific antigen-detection ELISA for the diagnosis of human neurocysticercosis. Trans. R. Soc. Trop. Med. Hyg. 92, 411–414. https://doi.org/10.1016/S0035-9203(98)91069-0.
Gustafsson, F., Steensgaard-Hansen, F., Badskjær, J., Poulsen, A.H., Corell, P., Hildebrandt, P., 2005. diagnostic and prognostic performance of N-terminal ProBNP in primary care patients with suspected heart failure. J. Card. Fail. 11, S15–S20. https://doi.org/10.1016/j.cardfail.2005.04.022.
Hancock, K., Tsang, V.C.W., 1986. Development and optimization of the FAST-ELISA for detecting antibodies to Schistosoma mansoni. J. Immunol. Methods 92, 167–176. https://doi.org/10.1016/0022-1759(86)90162-6.
Hess, L.H., 2013. Graphene Transistors for Biosensing and Bioelectronics. In: Proceedings IEEE 101, pp. 1780–1792. ⟨https://doi.org/10.1109/JPROC.2013.2261031⟩.
Hess, L.H., Seifert, M., Garrido, J.A., 2013. Graphene transistors for bioelectronics. In: Proceedings IEEE 101, pp. 1780–1792. ⟨https://doi.org/10.1109/JPROC.2013.2261031⟩.
Hnasko, R., Lin, A., McGarvey, J.A., Stanker, L.H., 2011. A rapid method to improve protein detection by indirect ELISA. Biochem. Biophys. Res. Commun. 410, 726–731. https://doi.org/10.1016/j.bbrc.2011.06.005.
Jorio, A., Saito, R., Dresselhaus, G., Dresselhaus, M.S., 2011. Raman Spectroscopy in Graphene Related Systems, Raman Spectroscopy in Graphene Related Systems. ⟨https://doi.org/10.1002/9783527632695⟩.
Kim, D.J., Sohn, I.Y., Jung, J.H., Yoon, O.J., Lee, N.E., Park, J.S., 2013. Reduced graphene oxide field-effect transistor for label-free femtomolar protein detection. Biosens. Bioelectron. 41, 621–626. https://doi.org/10.1016/j.bios.2012.09.040.
Li, H., Yin, X., Sun, D., Xia, K., Kang, C., Chu, S., Zhang, P., Wang, H., Qiu, Y., 2016. Detection of NT-pro BNP using fluorescent protein modified by streptavidin as a label in immunochromatographic assay. Sens. Bio-Sens. Res. 11, 1–7. https://doi.org/10.1016/j.sbsr.2016.08.001.
Li, P., Song, Y., Chen, S., Zhang, M., Wang, L., 2013. A novel biosensor based on acetylecholinesterase/chitosan-graphene oxide modified electrode for detection of carbaryl pesticides. Asian J. Chem. 25, 4444–4448.
Lu, X., Munief, W.M., Heib, F., Schmitt, M., Britz, A., Grandthyl, S., Müller, F., Neurohr, J.U., Jacobs, K., Benia, H.M., Lanche, R., Pachauri, V., Hempelmann, R., Ingebrandt, S., 2018a. Front-end-of-line integration of graphene oxide for graphene-based electrical platforms. Adv. Mater. Technol. https://doi.org/10.1002/admt.201700318.
Lu, X., Moidek, A., Munief, W.M., Jolly, P., Pachauri, V., Estrala, P., Ingebrandt, S., 2018b. Reduced graphene-oxide transducers of biosensing applications beyound the debye-screening limit. Biosens. Bioelectron. https://doi.org/10.1016/j.bios.2018.09.045.
Maisel, A.S., 2001. B-type natriuretic peptide (BNP) levels: diagnostic and therapeutic potential. Rev. Cardiovasc. Med. 2 (Suppl. 2), S13–S18.
Mao, S., Yu, K., Lu, G., Chen, J., 2011. Highly sensitive protein sensor based on thermally-reduced graphene oxide field-effect transistor. Nano Res. 4, 921–930. https://doi.org/10.1007/s12274-011-0148-3.
Morozov, S.V., Novoselov, K.S., Schedin, F., Jiang, D., Firsov, A.A., Geim, A.K., 2005. Two-dimensional electron and hole gases at the surface of graphite. Phys. Rev. B - Condens. Matter Mater. Phys. 72. https://doi.org/10.1103/PhysRevB.72.201401.
Munief, W.-M., Heib, F., Hempel, F., Lu, X., Schwartz, M., Pachauri, V., Hempelmann, R., Schmitt, M., Ingebrandt, S., 2018. Silane deposition via gas-phase evaporation and high-resolution surface characterization of the ultrathin siloxane coatings (8b01044.). Langmuir. https://doi.org/10.1021/acs.langmuir.8b01044.
Nair, R.R., Blake, P., Grigorenko, A.N., Novoselov, K.S., Booth, T.J., Stauber, T., Peres, N.M.R., Geim, A.K., 2008. Fine structure constant defines visual transperency of graphene. Science 320 (80-.), 2008. https://doi.org/10.1126/science.1156965.
Novoselov, K.S., Fal'Ko, V.I., Colombo, L., Gellert, P.R., Schwab, M.G., Kim, K., 2012. A roadmap for graphene. Nature. https://doi.org/10.1038/nature11458.
Pan, Y., Li, D., Ma, J., Shan, L., Wei, M., 2017. NT-proBNP test with improved accuracy for the diagnosis of chronic heart failure. Medicine 96, e9181. https://doi.org/10.1097/MD.0000000000009181.
Partoens, B., Peeters, F.M., 2006. From graphene to graphite: electronic structure around the K point. Phys. Rev. B - Condens. Matter Mater. Phys. 74. https://doi.org/10.1103/PhysRevB.74.075404.
Phan, D.-T., Chung, G.-S., 2015. Effects of rapid thermal annealing on humidity sensor based on graphene oxide thin films. Sens. Actuators B Chem. 220, 1050–1055. https://doi.org/10.1016/j.snb.2015.06.055.
Rani, D., Pachauri, V., Mueller, A., Vu, X.T., Nguyen, T.C., Ingebrandt, S., 2016. On the use of scalable NanoISFET arrays of silicon with highly reproducible sensor performance for biosensor applications. ACS Omega 1, 84–92. https://doi.org/10.1021/acsomega.6b00014.
Raphael, C., Briscoe, C., Davies, J., Whinnett, Z.I., Manisty, C., Sutton, R., Mayet, J., Francis, D.P., 2007. Limitations of the new York heart Association functional classification system and self-reported walking distances in chronic heart failure. Heart 93, 476–482. https://doi.org/10.1136/hrt.2006.089656.
Sabzwari, R., Slade, D.H., 2017. Stroke and infection: tuberculosis, brucellosis, syphilis, lyme disease and listeriosis, In: Primer on Cerebrovascular Diseases: Second Edition. pp. 635–641. ⟨https://doi.org/10.1016/B978-0-12-803058-5.00123-5⟩.
Saenger, A.K., Rodriguez-Fraga, O., Ler, R., Ordonez-Llanos, J., Jaffe, A.S., Goetze, J.P., Apple, F.S., 2017. Specificity of B-type natriuretic peptide assays: cross-reactivity with different BNP, NT-proBNP, and proBNP peptides. Clin. Chem. 63, 351–358. https://doi.org/10.1373/clinchem.2016.263749.
Schmitt, M., 2014. Analysis of silanes and of siloxanes formation by Raman spectroscopy. RSC Adv. 4, 1907–1917. https://doi.org/10.1039/C3RA45306E.
Schmitt, M., Heib, F., 2013. High-precision drop shape analysis on inclining flat surfaces: introduction and comparison of this special method with commercial contact angle analysis. J. Chem. Phys. 139. https://doi.org/10.1063/1.4822261.
Seshadri, P., Manoli, K., Schneiderhan-Marra, N., Anthes, U., Wierzchowiec, P., Bonrad, K., Di Franco, C., Torsi, L., 2018. Low-picomolar, label-free procalcitonin analytical detection with an electrolyte-gated organic field-effect transistor based electronic immunosensor. Biosens. Bioelectron. 104, 113–119. https://doi.org/10.1016/j.bios.2017.12.041.
Socrates, G., 2004. Infrared and Raman Characteristic Group Frequencies, Infrared and Raman characteristic group frequencies. ⟨https://doi.org/10.1002/jrs.1238⟩.
Song, K.S., Nimse, S.B., Sonawane, M.D., Warkad, S.D., Kim, T., 2017. Ultra-sensitive NT-proBNP quantification for early detection of risk factors leading to heart failure. Sensors 17. https://doi.org/10.3390/s17092116.
Stebunov, Y.V., Aftenieva, O.A., Arsenin, A.V., Volkov, V.S., 2015. Highly sensitive and selective sensor chips with graphene-oxide linking layer. ACS Appl. Mater. Interfaces 7, 21727–21734. https://doi.org/10.1021/acsami.5b04427.
Wang, Y., Li, Z., Wang, J., Li, J., Lin, Y., 2011. Graphene and graphene oxide: biofunctionalization and applications in biotechnology. Trends Biotechnol. https://doi.org/10.1016/j.tibtech.2011.01.008.
Zhang, J., Shu, Y.G., 2017. Highly sensitive detection of NT-proBNP by molecular motor. Genes Dis. 4, 37–40. https://doi.org/10.1016/j.gendis.2016.11.002.
Zhuo, Y., Yi, W.J., Lian, W.B., Yuan, R., Chai, Y.Q., Chen, A., Hu, C.M., 2011. Ultrasensitive electrochemical strategy for NT-proBNP detection with gold nanochains and horseradish peroxidase complex amplification. Biosens. Bioelectron. 26, 2188–2193. https://doi.org/10.1016/j.bios.2010.09.033.